

# X-Ray Enhancement Based on Component Attenuation, Contrast Adjustment, and Image Fusion

Ching-Chun Huang<sup>ID</sup>, Member, IEEE, and Manh-Hung Nguyen<sup>ID</sup>, Member, IEEE

**Abstract**—Inspecting X-ray images is an essential aspect of medical diagnosis. However, due to an X-ray’s low contrast and low dynamic range, important aspects such as organs, bones, and nodules become difficult to identify. Hence, contrast adjustment is critical, especially because of its ability to enhance the details in both bright and dark regions. For X-ray image enhancement, we therefore propose a new concept based on component attenuation. Notably, we assumed an X-ray image could be decomposed into tissue components and important details. Since tissues may not be the major primary focus of an X-ray, we proposed enhancing the visual contrast by adaptive tissue attenuation and dynamic range stretching. Via component decomposition and tissue attenuation, a parametric adjustment model was deduced to generate many enhanced images at once. Finally, an ensemble framework was proposed for fusing these enhanced images and producing a high-contrast output in both bright and dark regions. We have used measurement metrics to evaluate our system and achieved promising scores in each. An online testing system was also built for subjective evaluation. Moreover, we applied our system to an X-ray data set provided by the Japanese Society of Radiological Technology to help with nodule detection. The experimental results of which demonstrated the effectiveness of our method.

**Index Terms**—X-ray image enhancement, component attenuation, ensemble framework, parametric contrast adjustment model.

## I. INTRODUCTION

INSPECTING X-ray images is an important step for medical diagnosis. However, low contrast and low dynamic

Manuscript received June 8, 2017; revised February 2, 2018 and July 21, 2018; accepted July 23, 2018. Date of publication August 16, 2018; date of current version September 19, 2018. This work was supported in part by the Ministry of Science and Technology, Taiwan, under Grant 107-2811-E-194-002, Grant 107-2634-F-009-007, and Grant 106-2628-E-194-002-MY3, in part by the Center for Innovative Research on Aging Society (CIRAS), National Chung Cheng University, and in part by the Advanced Institute of Manufacturing with High-tech Innovations (AIM-HI) from The Featured Areas Research Center Program within the framework of the Higher Education Sprout Project by the Ministry of Education (MOE) in Taiwan. The associate editor coordinating the review of this manuscript and approving it for publication was Prof. Chia-Wen Lin. (*Corresponding author: Ching-Chun Huang*.)

C.-C. Huang is with the Department of Electrical Engineering, Advanced Institute of Manufacturing with High-tech Innovations, National Chung Cheng University, Minhsiu 62102, Taiwan, and also with the Center for Innovative Research on Aging Society, National Chung Cheng University, Minhsiu 62102, Taiwan (e-mail: chingchun.huang6@gmail.com).

M.-H. Nguyen is with the Department of Electrical Engineering, University of Technology and Education, Ho Chi Minh 777777, Vietnam, and also with the Department of Electrical Engineering, National Chung Cheng University, Minhsiu 62102, Taiwan (e-mail: nmhung.spkt@gmail.com).

Color versions of one or more of the figures in this paper are available online at <http://ieeexplore.ieee.org>.

Digital Object Identifier 10.1109/TIP.2018.2865637

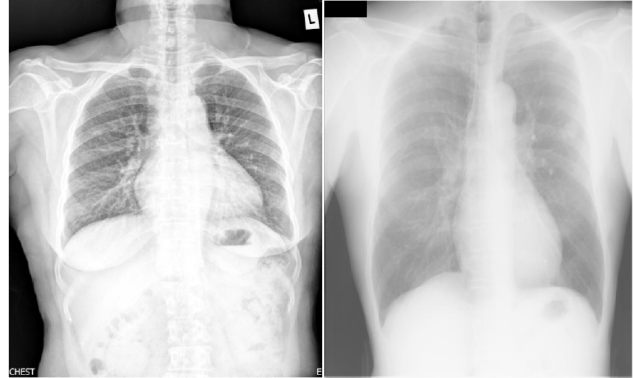


Fig. 1. Two typical X-ray images in our testing dataset. The images have low dynamic ranges. Their bright and dark regions also show low contrast.

range of an X-ray image make these body parts embedded in the bright or dark regions difficult to identify. The bright regions of an X-ray image are of interest because many important organs and bones are located here. In contrast, tiny but significant details, such as nodules usually appear in the dark regions. To identify organs and nodules simultaneously, a higher dynamic range is needed to clearly characterize both the bright and dark regions. Without enhancement, it is challenging to show details in a standard and low-dynamic-range (LDR) X-ray image.

Examples of X-ray images offered by a local hospital are shown in Fig. 1. The low contrast and the low dynamic range of these images make it hard to see the details and to make a correct diagnosis. To help with this, we propose an ensemble framework, which consists of tissue attenuation, contrast adjustment, and image fusion, for X-ray image enhancement. By increasing the contrast in bright regions and dark regions, our system aims to clearly present the details in LDR X-ray images apparently.

As we will discuss in Section II, many previous methods have been proposed to enhance an image’s contrast, such as global tone mapping [1], local adaptive tone mapping [2]–[4], Retinex-based methods [5]–[8], and transform-based methods [10]. These works are closely related to tone mapping that reduces the dynamic range of an HDR image and produces a contrast-enhanced LDR image. Similarly, our proposed method also relies on the concept of tone mapping to increase the local contrast. However, compared with the previous works, there are several differences in the design methodology. Below, we summarize the differences and contributions of our method.

A different way to enhance an X-ray image is presented in this paper. Instead of merely applying tone mapping, we anticipate more properties can be designed for X-ray image enhancement. First of all, component attenuation is proposed in our image contrast enhancement model. We know that the human body is made up of varying amounts of different tissue in different regions. Hence, we may assume that the intensity of the acquired image is based on tissue composition and other important details. However, too much tissue may make an acquired image become overly bright or foggy. Since tissue may not be the primary focus of an X-ray image, the visual contrast of image details could be greatly enhanced by tissue attenuation followed by dynamic range stretching. Thus, we propose designing an image processing method to enhance images by reducing some amounts of tissue components from images.

In our method, the extraction of maximum removable tissue components for enhancement was formulated as a contrast maximization problem. Later on, our system generated some enhanced images with different degrees of visualization by adjusting the level of tissue attenuation and stretching the contrast. Specifically, to generate these enhanced images, we formulated a parametric contrast adjustment model based on the concept of component attenuation. By inputting selected attenuation factors into the parametric adjustment model, the proposed system can efficiently generate enhanced images. Finally, we adopted an ensemble strategy to integrate many enhanced images. By determining suitable weights for image fusion, our ensemble framework is able to produce a final result with high contrast.

To the best of our knowledge, few works have ever applied component attenuation to X-ray image enhancement. In some sense, we might relate the proposed work to “dehazing” algorithms [9]. If the removable components are treated as the “haze” that reduces the contrast of an X-ray image, we can expect to have better visualization after component attenuation. Even so, the design of our method is entirely different from dehazing methods. For instance, instead of removing all haze, our enhancement model focuses on partially removing tissue components. In fact, the concept of component attenuation was initially proposed by Huang *et al.* [10], which is the early version of the current work. Even though the experimental results have demonstrated the effectiveness of the method [10] for enhancement, the brightness of the output image is reduced. For the bright regions of an X-ray image, the side effect might be negligible. However, the phenomenon makes dark regions darker and decreases the discriminability for X-ray inspection. To solve the problem, in this work, we propose a more general enhancement model. The model was designed to be capable of stretching the contrast in both bright and dark regions. While designing the adjustment model, we introduced a constraint for brightness consistency in order to preserve the local brightness of the original X-ray image. Furthermore, in Section III, we would show that the model used in [10] is a special case of our new model.

The rest of this paper is organized as follows. A survey and a summary of related works are introduced in Section II. In Section III, we derive the new image contrast enhancement

model based on component attenuation and analyze its function related to enhancing X-ray images. In Section IV, we then parametrize the enhancement model and explain the function of each model parameter. Next, via the parametric enhancement model, in Section V, we illustrate the proposed ensemble framework for X-ray enhancement. At the end of this section, we also summarize the implementation steps of our system in Algorithm 1 to offer a clear system overview. The discussions and experimental results are given in section VI. In section VII, we conclude this paper. As a supplement, we also summarize the mathematical symbols used in the paper in Appendix A. Appendix B and Appendix C include some deduction details of the proposed method.

## II. RELATIVE METHODS

Many image enhancement methods have been proposed for improving image contrast and details. The global tone mapping methods follow a mapping function to transfer input intensity values into new values while enlarging the global contrast, yet a typical drawback is that image details may be sacrificed. In contrast, local adaptive tone mapping methods follow spatially varying transfer functions to enhance contrast details [3], [4]. However, the results might produce undesirable block effects. Thus, maintaining spatial consistency after enhancement over local patches is a crucial issue. The Retinex theorem [5] suggests suppressing the bias of illumination in order to enhance local contrast [6]–[8]. For low illumination or dark regions, these Retinex-based methods are able to improve results. However, the output contrast is typically weak when dealing with bright regions. Moreover, the enhanced results usually have halo effects and look unnatural. On the other hand, transform-based methods apply transformations (such as DCT-discrete cosine transform or wavelet transform) to an image. The coefficients in a transform domain are then modified in accordance with the enhancement algorithms. Finally, the final enhanced image is obtained by an inverse transform. Although transform-based methods are able to accomplish global and local contrast enhancement, we may find halo effects in the output images. To reduce halo effects, some edge-preserving methods such as bilateral filtering [11] have recently been integrated with the transform-based methods.

For better understanding, we will summarize some relative and representative enhancement methods. Gamma correction [1], S-curve correction [12], and histogram equalization [1] are well-used global tone mapping methods. By manually selecting the gamma parameter of the global mapping function, gamma correction methods can stretch image contrast in either dark regions or bright regions. The idea behind S-curve correction methods is similar to gamma correction. However, S-curve correction methods provide more parameters for manual tuning and thus allow a system to use an S-shaped global mapping function for enhancing both dark and bright regions at the same time. On the other hand, histogram equalization (HE) [1] and multi-scale HE [13] aim to automatically determine the global mapping function by maximizing the histogram entropy of the enhanced image. HE-based methods are efficient but they tend to overly enhance an image and give unnatural

artifacts when the histogram distribution has peaks. Finally, these global tone mapping methods cannot adaptively enhance local image regions.

To improve local contrast, 2D-histogram-based mapping approaches [14]–[16] which introduce contexture information from the neighboring patches have been recently proposed. The key idea behind them is that the increase in the gray-level difference between a pixel and its neighbors could directly expand image local contrast. Accordingly, in [14], the author created a 2D histogram to record the occurrence of gray-level pairs within a small region. A mapping function could be established to equalize the 2D histogram in a way that makes the difference in intensity of neighboring pixel pairs uniformly distributed. Contextual and variational contrast enhancement algorithm (CVC) [15] is an improved version of [14]. As well as requiring the target histogram to be uniform, in CVC, a differential term was introduced to make the target histogram smooth. The final mapping function can be obtained by mapping the diagonal components of the original 2D histogram of the input image to the diagonal components of the 2D target histogram. In [16], a more complicated objective function was proposed to estimate the target histogram. Besides the uniform distribution constraint and smoothness constraints, higher order image factors have been simultaneously considered. These modifications may generate more satisfying results. However, the computation cost is high.

On the other hand, a hybrid strategy combining global mapping and transform-based enhancement was proposed in [17] and [18]. In [17], a spatial entropy-based contrast enhancement algorithm in DCT (SECEDCT) was introduced. The spatial entropy of different gray-level intensities over an image was defined and calculated. With the spatial entropy function, the global contrast enhancement function that maps the input intensity to an output value was then determined. Furthermore, to achieve local contrast enhancement, 2D-DCT was used to transfer the global enhanced image into the frequency domain. By appropriately weighting the high-frequency components, a globally and locally enhanced result can be obtained by an inverse transform of DCT. Although SECEDCT can enhance image contrast, the algorithm does not allow the system to control the level of global contrast and cannot preserve image brightness. To address these issues, the authors have recently proposed a modified version [18].

Retinex-based methods are other alternatives for image sharpening and dynamic range compression. Single-Scale Retinex (SSR) [8] enhances image contrast by calculating the intensity ratio between a pixel and its surroundings. However, to get a better result, it requires a trial-and-error process to select the filter scale. Furthermore, to balance dynamic compression and image rendering, Multi-Scale Retinex (MSR) [9] was proposed to fuse many SSR-enhanced results generated under different filter scales.

Retinex-based methods and transform-based methods are related. Both methods decompose an input image into base layers (low-frequency components) and detail layers (high-frequency components). By attenuating the base layers or boosting the detail layers, the image details can be

identified. Different decomposition strategies have been found in the literature. Choi *et al.* [19], Durand and Dorsey [20] enhanced an image using one base layer and one detail layer, whereas multiple base and detail layers were considered for enhancement in [21]–[24]. In particular, linear functions were used to compress the base layers [21], [22] in the original intensity domain. Instead, [23], [24] compressed the dynamic range by nonlinear functions in the feature domain.

Recently, some ensemble frameworks have been proposed to improve the quality of an image. Instead of enhancing an image by means of a unified parameter setting, an ensemble-based method attempts to generate many improved versions in which some image parts show a higher perceptual quality than the original input. These generated images are then seamlessly combined to produce the final enhanced result. In [25], the authors used LLSURE filters to generate images with less noise. The final de-noised result was realized through average fusion. In order to render an HDR image and achieve HDR compression, Wang *et al.* [26], Huang *et al.* [27] proposed methods to synthesize many exposure images. However, without proper modifications, a weighted combination result may lead to intensity inconsistency between neighboring pixels. To avoid the inconsistency, multi-resolution blending methods based on a Laplacian pyramid [28]–[30] can be adopted to preserve the image contrast and ensure local intensity consistency. Although ensemble-based methods have achieved success for HDR image compression, few ensemble-based methods have been proposed for single image contrast enhancement, especially for X-ray images.

### III. IMAGE CONTRAST ENHANCEMENT MODEL

An image contrast enhancement model is proposed via component attenuation. We assumed that an X-ray image could be composed of removable and detail components. Here, the removable components refer to some amounts of body tissue. In contrast, the detail components consist of the portions of interest like bones and organs. In order to enhance an X-ray image, we attenuate the removable components so that we can extend the dynamic range to represent the detail components. To realize the concept, our image model is defined as:

$$I_n(x) = I(x) / I_{max} = D(x) + R(x), \quad (1)$$

where  $I_n(x)$  is a normalization image,  $I(x)$  is the input X-ray image,  $I_{max}$  is the maximum value of the whole image,  $D(x)$  is the detail component, and  $R(x)$  is the removable part. Also,  $x$  is a spatial index,  $I_n(x)$ ,  $D(x)$ , and  $R(x)$  are all between 0 and 1. To achieve the final enhanced X-ray Image  $E(x)$ , a contrast enhancement function  $Ce(\cdot)$  is applied to the detail component  $D(x)$ . That is:

$$E(x) = Ce(D(x)) = Ce(I_n(x) - R(x)). \quad (2)$$

After removing  $R(x)$  from  $I_n(x)$ , as shown in Fig. 2, it is expected that we have free space to enhance  $D(x)$  by enlarging its dynamic range. If we can design the enhancement function  $Ce(\cdot)$  to utilize the free dynamic range, image enhancement becomes possible.

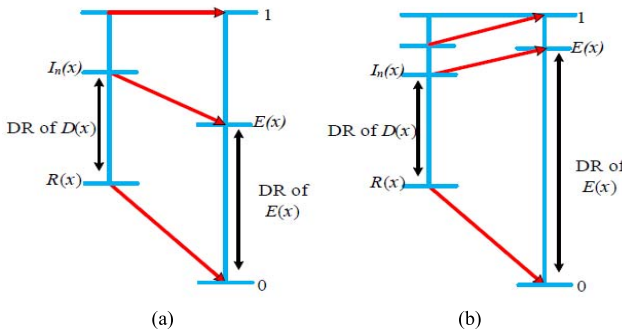


Fig. 2. (a) The concept of our enhancement method for  $\lambda(x) = 0$ , same setting in [10]; (b) The concept of the proposed method for  $\lambda(x) = 1$ . DR means “Dynamic Range”. Please also refer the main text for the notations.

In our system, the designed enhancement function  $Ce(\cdot)$  is

$$E(x) = Ce(D(x)) = \frac{I_n(x) - R(x)}{I_n^{\max}(x)^{\lambda(x)} - R(x)}. \quad (3)$$

Here,  $I_n^{\max}(x) = \max_{y \in L_x} I(y)$  is the local maximum of the local region,  $L_x$ , around the image pixel  $x$ , and  $\lambda(x)$  is a controllable parameter. The derivation of  $\lambda(x)$  is explained in Section IV. Ideally,  $\lambda(x)$  helps to flexibly adjust the reference level in our enhancement model. To bind the range of  $\lambda(x)$ , we decided to introduce  $\lambda(x)$  in the exponential term. While we set  $\lambda(x) = 0$ , as shown in Fig. 2(a), our model degenerates into the early method proposed in [10]. If  $\lambda(x) = 1$ , the model  $E(x)$  degrades to refer to the local maximum  $I_n^{\max}(x)$ . As shown in Fig 2(b), the dynamic range of  $E(x)$  in this case is evidently enlarged when compared with the dynamic range in Fig 2(a).

The proposed model not only makes the enhanced image more brilliant but also makes the contrast stronger. As Fig 2(b) reveals, for a location  $x$ , the intensity value of our enhanced result  $E(x)$  can be larger than  $I_n(x)$ ; thus, the enhanced image can be more brilliant. Moreover, since the maximum value of  $E(x)$  is not limited by  $I_n(x)$ , the dynamic range of the enhanced image can be broadened. In addition, by referring to the local maximum  $I_n^{\max}(x)$ , the proposed method can strengthen the contrast in both dark and bright regions. The property can be further explained by understanding equation (3). In particular, the contrast stretch is controlled by  $1/(I_n^{\max}(x)^{\lambda(x)} - R(x))$ . For a dark region, the denominator,  $I_n^{\max}(x)^{\lambda(x)} - R(x)$ , is also small. Hence, the contrast can be stretched. For a bright region,  $I_n^{\max}(x) \approx 1$ , and therefore the enhancement of  $E(x)$  is similar to the result produced by [10], which has shown its ability to well enhance bright regions.

So far, we have explained the key idea of using component attenuation for contrast enhancement. In the next section, we will introduce the complete formulation for enhancement where we systematically parametrize the proposed contrast adjustment model, deduce the attenuation component  $R(x)$ , and determine the term  $\lambda(x)$ .

#### IV. PARAMETRIC CONTRAST ADJUSTMENT

The attenuation component  $R(x)$  in equation (1) plays a key role in our contrast enhancement model. Suppose that the maximum removable tissue component map for image contrast enhancement can be determined and denoted as  $T(x)$ . We could set  $R(x) = T(x)$  to remove as much tissue as possible and greatly stretch the image contrast in order to get a highly enhanced result. However, the tissue could be muscle or fat. Organs are also made of body tissue. If removing too much tissue for contrast stretching, we may also lose useful contents. Thus, in our system, we only attenuated partial components.

In our method, to determine the attenuation component  $R(x)$ , we introduced an attenuation factor,  $\alpha$ , and defined  $R(x) \equiv \alpha \cdot T(x)$  to control the ratio for component removal. By estimating the maximum removable tissue component map  $T(x)$  and controlling  $\alpha$ , we can determine  $R(x)$  so as to enhance an X-ray image properly. Since the contrast enhancement level is highly relevant to the amount of removed tissue,  $\alpha$  becomes the main parameter of our parametric contrast adjustment model. We also treat  $\alpha$  as a global parameter in our parametric model since the setting of  $\alpha$  is invariant to pixel locations. To be clear, in Section VI.A, we will discuss the selection of the attenuation factor. Furthermore, we analyze more insights of component attenuation for contrast adjustment in Appendix B.

The second controllable term in our model is  $\lambda(x)$  which is defined in equation (3). By introducing  $\lambda(x)$ , our model can be adjusted to satisfy preferred image constraints. Unlike  $\alpha$ ,  $\lambda(x)$  changes locally. In our system, we locally adjust the value of  $\lambda(x)$  at different locations in order to keep the brightness consistent. Below, we illustrate the determination of  $T(x)$  and the calculation of the term  $\lambda(x)$ .

##### A. The Maximum Removable Tissue Component Map, $T(x)$

Without extra information, the decomposition of  $T(x)$  from an X-ray image is a difficult problem to solve. To estimate  $T(x)$ , we introduced a constraint which is named “Local Contrast Maximization”. If we set  $R(x) = T(x)$ , that is  $\alpha = 1$ , to stretch the local contrast, an extremely high contrast result would be produced. To explain the idea, the stretching results under  $R(x) = T(x)$  and  $R(x) = \alpha \cdot T(x)$  are given in Fig. 3(a) and Fig. 3(b) separately. When  $R(x) = T(x)$ , the dynamic range is obviously maximized. To further verify the assumption, some enhanced images for different  $\alpha$  values are provided in Fig. 5. When  $\alpha = 1$ , the image is apparently over-enhanced if compared with other enhanced results.

Based on the “Local Contrast Maximization” constraint, the map  $T(x)$  could be determined by finding the optimal removable component map which maximizes the summation of local contrast over the final enhanced image  $E$ . Accordingly, to determine  $T(x)$ , we defined and solved the corresponding optimization problem. The derivation detail is illustrated in Appendix C which shows the map  $T$  could be approximated well by equation (4).

$$T(x) \cong \min_{y \in L_x} I_n(y) \triangleq I_n^{\min}(x). \quad (4)$$

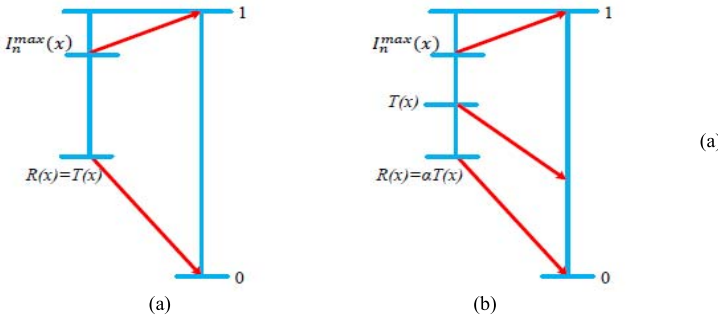


Fig. 3. The stretching diagrams of the dynamic range when: (a) removing the maximum removable component  $R(x) = T(x)$ ; and (b) properly attenuating the amount of removable tissues  $R(x) = \alpha \times T(x)$ .  $\lambda(x)=1$  for the two cases.

In (4),  $L_x$  represents the local region around the pixel  $x$ , and  $y$  is a pixel inside  $L_x$ . Thus, the component map  $T(x)$  at pixel  $x$  can be estimated by finding the local minimum within a local region around  $x$ . In our implementation, considering system efficiency, we used a  $7 \times 7$  window to approximate the local image region.

### B. Contrast Enhancement With Brightness Consistency

It can be shown that the attenuation factor  $\alpha$  allows us to globally control the contrast enhancement ratio between a normalized image  $I_n(x)$  and its enhanced result  $E(x)$ . That is  $\frac{LCR(E(x))}{LCR(I_n(x))} = \frac{1}{1-\alpha}$ , whose derivation details can be found in Appendix B. The equation tells that the contrast enhancement ratio is fixed to  $\frac{1}{1-\alpha}$  for all image pixels. Thus, the  $\alpha$  value is treated as a global parameter in our method. In the equation, the  $LCR(\cdot)$  function calculates a local patch contrast ratio ( $LCR$ ) which is also known as Weber local contrast [31].

However, the contrast enhancement ratio is not the only factor that influences image enhancement. An example is shown in Fig. 4. Fig. 4(a) shows the original image. Fig. 4(b) and 4(c) are the results based on the proposed enhancement model. The  $\alpha$  values used for Fig. 4(b) and 4(c) are equal, but the settings of  $\lambda(x)$  are different. In Fig. 4(b),  $\lambda(x)$  is 0, whereas  $\lambda(x)$  is 0.7 for Fig. 4(c). Due to having the same  $\alpha$  value, the enhancement ratios of the two enhanced images should be equal. However, Fig. 4(b) and 4(c) show apparent differences in brightness. From equation (3), we see the difference comes from the scaling term  $I_n^{max}(x)^{\lambda(x)} - R(x)$ . Thus, by altering the scaling term, we can adjust image local properties and also keep enhancement ratio same. Specifically, the parameter  $\lambda(x)$  provides our model with the flexibility to control local image brightness.

However, without a correct setting of  $\lambda(x)$ , the result may not be good. Examples can be found in Fig. 4. For  $\lambda(x) = 0$ , the enhanced images become darker, as shown in Fig. 4(b), whereas the enhanced images tend to be locally over-bright for  $\lambda(x) = 0.7$ , as shown in Fig. 4(c). Thus, we still need to find a suitable setting of  $\lambda(x)$  to keep the consistency of image local brightness. In our system, we then require the maximum image value in a local area  $L_x$  to be kept at the same level after image enhancement. Thus, the brightness property can be maintained locally. This leads to our brightness consistency

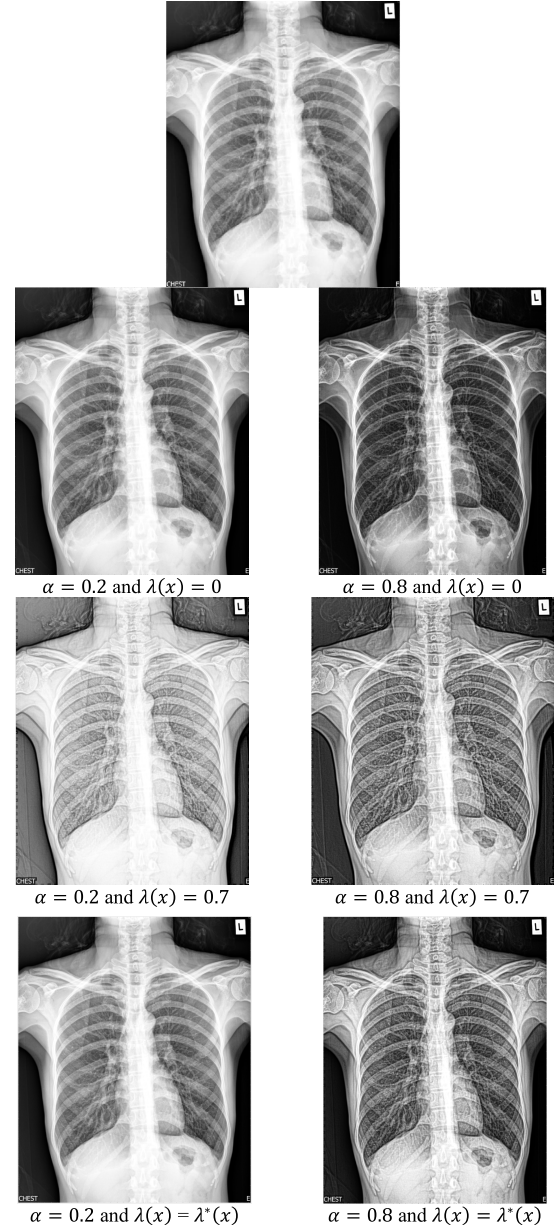


Fig. 4. (a) The original images; (b) and (c) are the enhanced results under  $\lambda(x) = 0$  and  $\lambda(x) = 0.7$ ; (d) shows the enhanced results under  $\lambda^*(x)$ , which is determined by equation (6).

constraint being defined as follows:

$$E_n^{max}(x) \triangleq \max_{y \in L_x} E(y) = I_n^{max}(x) \triangleq \max_{y \in L_x} I_n(y). \quad (5)$$

Now, given a global attenuation ratio  $\alpha$  and the brightness constraint described in (5), the selected parameter  $\lambda^*(x)$  at pixel  $x$  can be determined by equation (6):

$$\lambda^*(x) = \log \left[ 1 - \alpha I_n^{min}(x) \left( \frac{1}{I_n^{max}(x)} - 1 \right) \right] / \log (I_n^{max}(x)). \quad (6)$$

To derive equation (6), we have replaced  $E_n^{max}(x)$  in equation (5) by the equation (A.3) in Appendix B. Since the interval of  $\alpha$  is  $[0,1]$ , it can be proved by equation (6) that the interval of  $\lambda^*$  is also  $[0,1]$ . In some cases, the brightness of

the original X-ray image is globally compressed and therefore the brightness consistency becomes impractical. To solve the problem, a preprocessing step based on histogram equalization was introduced into our processing phase to globally stretch image histogram before applying the proposed main method.

## V. THE ENSEMBLE FRAMEWORK FOR IMAGE ENHANCEMENT

So far, given an attenuation ratio  $\alpha$ , we are able to generate an enhanced image by equation (3). Note that parameter  $\lambda(x)$  can be calculated using equation (6) and the attenuation component map  $R(x)$  is determined by  $R(x) \equiv \alpha \cdot T(x)$ . For reference, some enhanced images under different settings of  $\alpha$  are provided in Fig. 5. As Fig. 5 shows, the enhanced level is increased when we adjust  $\alpha$  from 0 to 1. This also matches the conclusion in Appendix B that  $\alpha$  allows us to control the enhancement ratio.

In addition, the selection of the attenuation ratio should be further discussed. When we attenuate tissue components, as shown in Fig. 5, the dynamic contrast of the image details is stretched. However, at the same time, some information in the enhanced image is missing, especially the low-frequency components. Therefore, it would be challenging to generate a satisfactory enhancement by selecting an optimal attenuation ratio to produce the final result. Instead, we proposed an image ensemble framework that not only offers a solution to produce a pleasing result by integrating many enhanced images but also keep our system efficient.

The proposed ensemble framework is presented in Fig. 6. For an input normalized image  $I_n(x)$ , we estimate the tissue component using equation (4), select  $K$  attenuation ratios  $\{\alpha_i\}_{i=1}^K$  in the interval  $[0,1]$ , and generate  $K$  enhanced images  $\{E_i(x)\}_{i=1}^K$ . To achieve the final output image, we combine the  $K$  enhanced images based on local image quality. For efficiency, we borrowed the idea from Exposure Fusion (EF) [32]. That is, given  $K$  enhanced images  $\{E_i(x)\}_{i=1}^K$ , our system generates the combined image  $F(x)$  by

$$F(x) = EF(\{E_i(x), W_i(x)\}_{i=1}^K). \quad (7)$$

In (7),  $EF(\cdot)$  represents the Exposure Fusion algorithm.  $W_i(x)$  is the weight map for the  $i^{\text{th}}$  enhanced image.  $x$  represents a pixel's location. Also, the summation of weights at one pixel over  $K$  images is required to be equal to 1. To determine the weight maps  $\{W_i(x)\}_{i=1}^K$ , we evaluated the image quality around each pixel in each individual image. The evaluation is based on two quality metrics: (a) contrast level; and (b) brightness preservation. The contrast level  $C_i(x)$  of the  $i^{\text{th}}$  enhanced image  $E_i$  at pixel  $x$  is measured by:

$$C_i(x) = \frac{|\Delta E_i(x)|}{E_i(x) + \varepsilon} = \frac{|E_i(x) * G_L|}{E_i(x) * G_A + \varepsilon}, \quad (8)$$

where the operator “\*” indicates image convolution.  $G_L$  is a standard  $5 \times 5$  Laplacian filter that helps to calculate the second order difference between a pixel and its neighbors;  $G_A$  is a  $5 \times 5$  Gaussian filter that helps to calculate the weighted average intensity around pixel  $x$ .  $\Delta E_i(x)$  and  $E_i(x)$  are convoluted images by  $G_L$  and  $G_A$  correspondently. An absolute

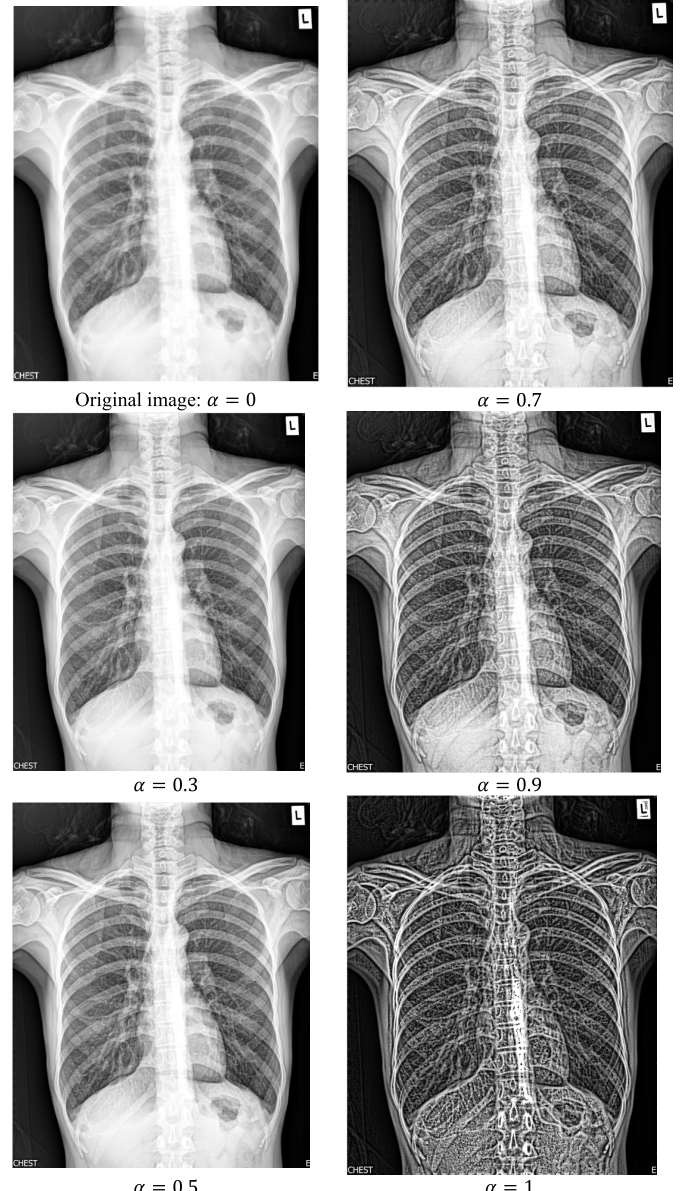


Fig. 5. One testing image and its enhanced images under different settings of  $\alpha$ . The corresponding parameter  $\lambda^*(x)$  was determined by equation (6).

operator is added in (8) to make sure  $C_i(x)$  is positive; we also add a small value  $\varepsilon$  in the denominator to avoid the division-by-zero problem when a pixel of the convoluted image  $E_i(x) * G_A$  approaches 0. In general, we would assign a high weight to a high contrast pixel.

In addition, we hoped that the fusion result  $F(x)$  preserves the local maximum brightness, like the brightness consistency constraint we used in equation (5). Hence, we introduced a brightness preservation metric  $BP_i(x)$ , defined in equation (9), to control the fusion weight at pixel  $x$  in the  $i^{\text{th}}$  enhanced image.

$$BP_i(x) = \exp\left(-\left(\frac{D_i(x)}{\sigma}\right)^2\right). \quad (9)$$

Here,  $D_i(x) = \max_{y \in L_x} E_i(y) - \max_{y \in L_x} I_n(y)$  represents the local maximum difference between the  $i^{\text{th}}$  enhanced image  $E_i(x)$

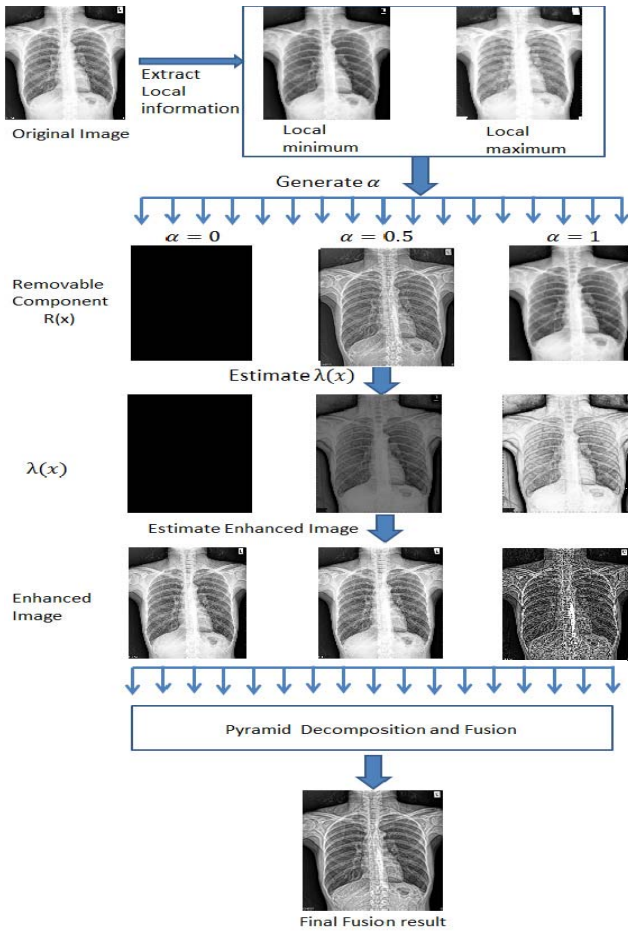


Fig. 6. The proposed ensemble framework for contrast enhancement.

and the original image  $I_n(x)$ .  $\sigma$  is the standard deviation of local maximum differences. In (9), a small  $D_i(x)$  means that the local maximum brightness can be preserved and therefore the corresponding  $BP_i(x)$  value is high. Otherwise, the  $BP_i(x)$  value would be low.

Finally, by combining  $C_i(x)$  and  $BP_i(x)$ , we determine the fusion weight  $W_i(x)$  at pixel  $x$  in the  $i^{\text{th}}$  enhanced image as:

$$W_i(x) = C_i(x) \times BP_i(x). \quad (10)$$

Later on, we input  $E_i(x)$  and  $W_i(x)$  into the Exposure Fusion algorithm [32] to produce the final fusion result. Here, the EF algorithm is able to seamlessly blend many enhanced images  $\{E_i^M(x)\}$  according to their weight maps  $\{W_i(x)\}$  via pyramid decomposition. To summarize, we clarify the implementation steps of our ensemble framework for X-ray enhancement in Algorithm 1. Some fusion results are given in Fig. 7. Based on the ensemble framework, the local image contrast is well presented and the image details are well preserved.

## VI. EXPERIMENTAL RESULTS AND DISCUSSIONS

To subjectively evaluate the proposed system, we built an online testing system [33] and invited some radiologists and doctors to test our system. The user feedback can be found in [34]. Furthermore, we created a google survey form [35]

### Algorithm 1 Ensemble Enhancement Procedure

**Input:** Original image ( $I$ ), number of generated images ( $K$ ).

**Output:** Final fusion result  $F(x)$

#### Algorithm

- 0: Pre-process: Apply histogram equalization to  $I$
- 1: Compute the normalized image ( $I_n$ ) by equation (1)
- 2: Estimate tissue component  $T(x) \approx I_n^{\min}(x)$
- 3: Select  $K$  attenuation factors  $\{\alpha_i\}_{i=1}^K$
- 4: **For each**  $\alpha_i$
- 5: Compute attenuation component  $R_i(x)$  based on  $R_i(x) \equiv \alpha_i \cdot T(x)$ .
- 6: Compute the parameter  $\lambda_i^*(x)$  based on equation (6).
- 7: Generate an enhanced image  $E_i(x)$  using equation (3).
- 8: Compute contrast level  $C_i(x)$  and brightness preservation metric  $BP_i(x)$  to estimate the fusion weight  $W_i(x)$  according to equations (9) and (10)
- 9: **End**
- 10: To produce the fusion result  $F(x)$ , fuse  $K$  enhanced images  $\{E_i^M(x)\}_{i=1}^K$  according to their weight maps  $\{W_i(x)\}_{i=1}^K$  via the Exposure Fusion algorithm [32].



Fig. 7. X-ray image enhancement based on the proposed method. The first row contains the original images; the second row shows the results.

to subjectively evaluate that whether the enhanced results of the proposed method are better than those of other methods. From these subject surveys, we can find the proposed method gains the most positive feedbacks.

On the other hand, for objective evaluation, we used discrete entropy (DE) [36], absolute mean brightness error (AMBE) [2], measurement of enhancement (EME) [37], and Tenengrad criterion (TEN) [38] for image quality measurement. The four metrics measure image quality according to different properties. DE is used to measure the information level of an image. A larger DE score means more image information can be kept. To measure the ability to preserve image brightness, we used the AMBE metric. A smaller AMBE means that the method preserves brightness better than a method with a higher value. In addition, EME measures the enhancement level of an enhanced image. A higher EME

implies better enhancement. For measuring sharpness, we used TEN. The criterion is based on gradient magnitude to evaluate image quality. A higher TEN value indicates that the image is sharper.

Two different datasets were utilized for system analysis, testing, and comparison. The first dataset was provided by a local hospital. There are 70 X-ray images in this dataset [33]. The other dataset is the Japanese Society of Radiological Technology (JSRT) dataset [39], which includes many chest X-ray images with tiny nodules around the lung area. We will analyze the experimental results of the proposed method in Section VI.A. The comparisons are presented in Section VI.B. Besides image enhancement, by using the JSRT dataset, we hope to show our system assists doctors in nodule inspection. The results, in Section VI.C., demonstrate that our system makes nodules recognizable in the low contrast regions.

#### A. Discussion of the Proposed System

In order to evaluate the effectiveness and robustness of the proposed method, we tested our system using many medical X-ray images. Some test images and enhanced results are shown in Fig. 7. As shown in Fig. 7, the original images are over bright, low contrast, and it's hard to see the details. Even so, by attenuating tissue components and applying our ensemble algorithm, we are able to strengthen the image contrast and reveal the details. Moreover, the proposed enhancement model involves pixel-wise computing only. Therefore, our system can be implemented in an efficient way. Currently, our algorithm is implemented on a PC with an Intel Core i5 3.0 GHz CPU and 4GB of memory. It takes about 0.2 seconds to process a standard X-ray image with an image resolution of  $640 \times 520$ .

In our system, some parameters should be set. Based on our analysis, we finally chose the following setting as default for most of our experiments and produce acceptable results.

- (a) The attenuation ratio set is  $\{0.5, 0.6, 0.7, 0.8, 0.9, 1.0\}$ .
- (b) The window size is  $7 \times 7$ .
- (c) 6 enhanced images are used for fusion.

However, to understand the proposed system in depth, it is worthwhile to know the effects of the parameter setting from three aspects: (1) the effect of attenuation ratios, (2) the effect of the neighborhood size, and (3) the number of enhanced images for result fusion. Below, we discuss the details.

*1) The Effect of Attenuation Ratios:* The selection of attenuation ratios for fusion is a key issue that needs to be discussed further. In the experiment, to understand the influence of different combinations of enhanced images, three attenuation ratio sets, as defined in Fig. 8, are tested. Each ratio set has 6 elements implying there are 6 enhanced images used for fusion. These ratio sets are selected in a uniform manner or in an exponential manner. One test example under these ratio sets is presented in Fig. 8. Also, we compare the fusion results under the three ratio sets by inspecting DE, AMBE, EME, and TEN. Both Table I and Fig. 8 show that the fusion results are not sensitive to the ratio sets. It may be because the proposed ensemble framework is able to automatically balance the strengths and the weaknesses among many enhanced images.

We also try to automatically determine the optimal ratio set. In this experiment, we applied Particle Swarm Optimization

TABLE I  
ENHANCEMENT COMPARISON UNDER DIFFERENT ATTENUATION RATIO SETS. THE METRICS ARE DISCRETE ENTROPY (DE), ABSOLUTE MEAN BRIGHTNESS ERROR (AMBE), MEASUREMENT OF ENHANCEMENT (EME), AND TENENGRAV CRITERION (TEN). SEE THE MAIN TEXTS FOR MORE DETAILS

Ratio Set	DE	AMBE	EME	TEN
1 <sup>st</sup> ratio set	7.7522	0.1006	19.5302	0.4671
2 <sup>nd</sup> ratio set	7.7385	0.0874	18.7089	0.4492
3 <sup>rd</sup> ratio set	7.7653	0.1148	20.4950	0.4872
Optimal ratio set	7.8257	0.1236	21.0731	0.4784

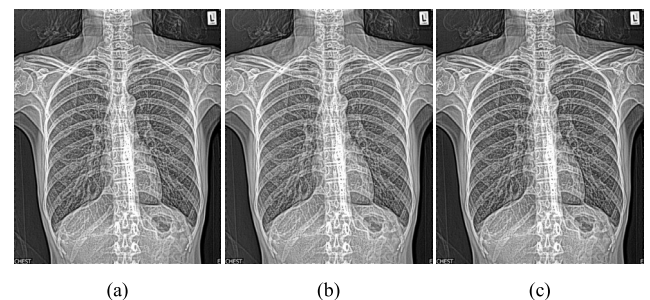


Fig. 8. Final fusion images under different attenuation ratio sets. (a) 1<sup>st</sup> ratio set  $\{0.5, 0.6, 0.7, 0.8, 0.9, 1\}$ . (b) 2<sup>nd</sup> ratio set  $\{0.5, 0.58, 0.63, 0.74, 0.82, 1\}$ . (c) 3<sup>rd</sup> ratio set  $\{0.5, 0.67, 0.79, 0.87, 0.92, 1\}$ .

(PSO) framework [40] to find the optimal ratio set. The objective function is to maximize the summation of the DE value, the EME value, the TEN value, and the negative AMBE value. Note that these metrics have different intensity ranges and should be normalized before evaluation. For the test sample in Fig. 8, 1000 particles are used and the found optimal ratio set is  $\{0.69, 0.79, 0.89, 0.92, 0.95, 0.98\}$ . The corresponding metric values are also listed in Table I for comparison. Although the result could be slightly improved, the optimization process is highly costly. In practical, we may directly use the default ratio set to generate acceptable results without optimization.

*2) The Effect of the Neighborhood Size:* The window size used in our system is another factor we need to analyze. To understand the details, an experiment is performed to enhance images under different window sizes. The corresponding final results are presented in Fig. 9. As the patch size increases, we find the sharpness is gradually reduced. Even so, the image brightness could be better preserved by using a larger size. To quantitatively analysis, we also calculate the four metrics DE, AMBE, EME, and TEN under different window sizes. Their values are presented in Table II. Here, the DE values under different sizes are roughly same; it means the proposed method is less sensitive to window sizes in terms of keeping image information level. In addition, the AMBE metric shows that a large size could well preserve image brightness. However, the table also reveals that a larger window size leads to lower enhance levels (EME) and image sharpness (TEN). To find a compromise between brightness

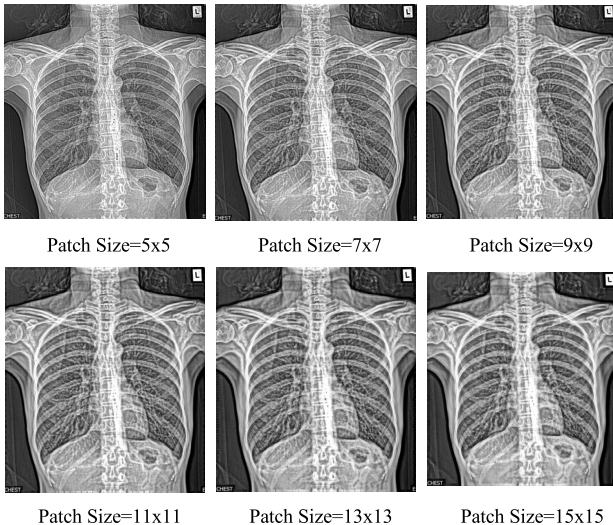


Fig. 9. Comparison of final fusion images using different window sizes.

TABLE II

PERFORMANCE UNDER DIFFERENT WINDOW SIZES. THE METRICS ARE DISCRETE ENTROPY (DE), ABSOLUTE MEAN BRIGHTNESS ERROR (AMBE), MEASUREMENT OF ENHANCEMENT (EME), AND TENENGRAV CRITERION (TEN)

Window Size	DE	AMBE	EME	TEN
5x5	7.7186	0.1164	20.442	0.5329
7x7	7.7522	0.1007	19.5303	0.4672
9x9	7.7780	0.0911	18.6802	0.408
11x11	7.7974	0.0841	17.8483	0.3638
13x13	7.8147	0.0786	16.8502	0.3284
15x15	7.8285	0.0748	16.0329	0.3006

and sharpness, we finally select  $7 \times 7$  as our default window size.

3) *The Number of Enhanced Images for Fusion:* Additionally, the number of enhanced images utilized for fusion should be analyzed. In our experiment, we compared the fusion results based on 4, 6, 8, 10, and 12 enhanced images. The distributions of TEN and DE over different numbers of images are shown in Fig. 10. The DE distribution shows that the information level of the final result tends to be saturated when using 6 or more images. On the other hand, the TEN distribution indicates that the sharpness of the fused image is gradually reduced as the number of image increases. To be compromised and efficient, we choose 6 images as a trade-off setting to implement our system.

#### B. Comparison of Contrast Enhancement

1) *Compare With Our Previous Work:* We compare the proposed method with our previous work [10] to show the improvement. Both models enhance images using the concept of component attenuation. However, based on the previous work [10] for enhancement, the brightness of the final result would decrease. In contrast, the newly proposed model can make the enhanced details more brilliant and the contrast stronger. We can check Fig. 11 and compare the difference

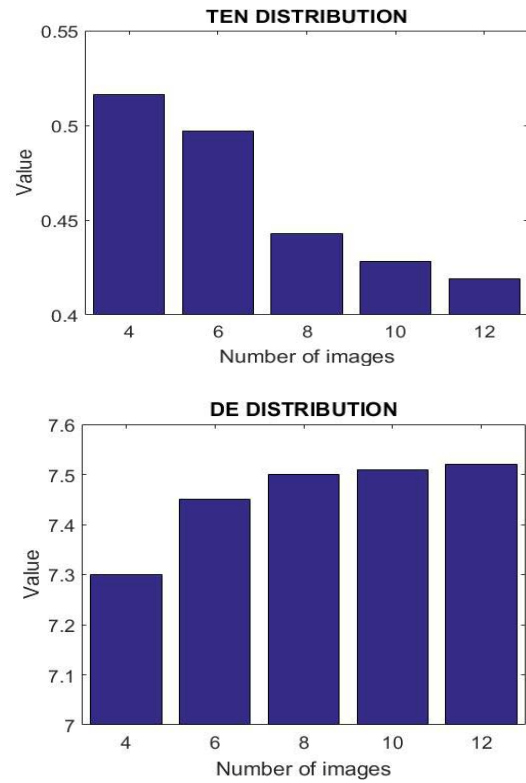


Fig. 10. The distributions of the TEN (Tenengrad criterion) and DE (discrete entropy) metrics over different numbers of enhanced images for fusion.

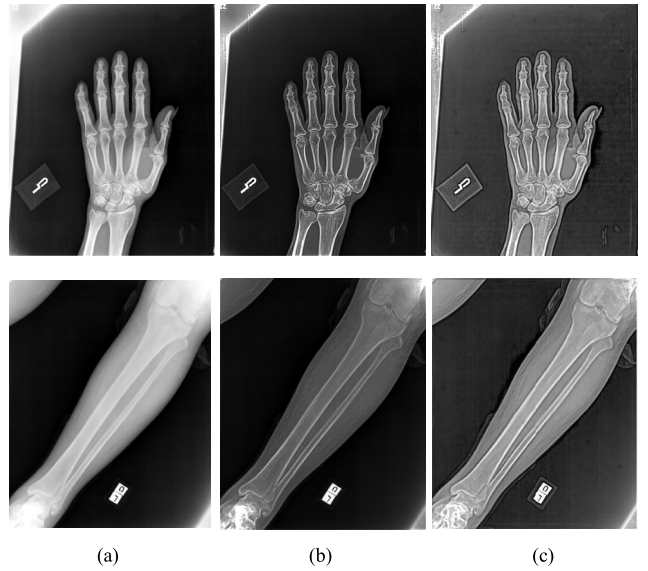


Fig. 11. A comparison of two contrast enhancement models. (a) The original images. (b) The results outputted by our previous model [10]. (c) The results produced by our method. Both models enhance images using the concept of component attenuation.

between the two models. Overall, both models give better visualization for X-ray inspection. However, the image brightness of our new model is higher. Furthermore, the proposed ensemble framework with the new parametric model provides clearer image details and a more uniform contrast enhancement.

As an aside, our previous model in [10] is designed specifically for the bright regions, but the dark regions are less enhanced. As our expectation, the details of the dark region in Fig. 11(b) are not as distinct as the ones in Fig. 11(c). In contrast, because the new model refers to the local maximum of an image region to adjust contrast, the result gives a better enhancement. Like Fig. 11(c), both dark and bright regions are well presented. If we quantitatively assess the two models, the mean ME value and the mean TEN value of the new proposed method over our first dataset are 20.5 and 0.59 respectively; in contrast, the mean ME and TEN produced by [10] are 11.06 and 0.18 respectively.

*2) Compare With Other Relative Works:* Two global contrast adjustment methods, gamma correction (GC) and histogram equalization (HE), were compared with our method. Meanwhile, eight state-of-the-art enhancement methods were also used for quality comparison. They are: spatial entropy-based global and local contrast enhancement (SEGL) [17], 2D histogram equalization (2D\_hist) [16], histogram-based locality-preserving (HBLP) [2], adaptive gamma correction (AGC) [4], bilateral filter (BF) [20], local and SURE-based edge-preserving (LL-SURE) method [25], luminance and contrast masking (LCM) [24], and tissue attenuation (TA) [10]. In total, 10 algorithms were considered for performance comparison.

We applied the 11 algorithms to the 70 images provided in the local hospital dataset [33] and produced the enhanced X-ray images. The aforementioned 4 performance metrics were calculated for each enhanced image. Next, the mean values of the metrics over the 70 images were compared (see Table III). According to the results in Table III, the proposed method achieves better results than most of the other methods.

To analyze the performance of these methods, we will discuss three aspects: enhancement quality, information level, and brightness preservation. To evaluate the quality of the enhancements, EME and TEN were used. As indicated in Table III, the EME and TEN values of our method were 20.55 and 0.59 respectively. They are also the highest values of all the methods. In addition, in Fig. 12, we show the distributions of the EME value over 70 enhanced images produced by BF [20], LLSURE [25], TA [10], and the proposed method. The distributions show that our system can enhance images better than the other three methods.

Histogram entropy is a common indicator usually used to measure the information level of an enhanced image. To know the information level of the enhanced images, we adopted the DE metric. In Table III, the DE values produced by the 11 methods are all high. This means that these methods can all utilize the image dynamic range well. It also means that the image intensities are widely distributed. Note that the DE value of the proposed method is 7.63, which is the highest of the 11 methods.

The final metric is AMBE. This measures the system's ability to preserve brightness. It should be noted that there is always a tradeoff between contrast enhancement and brightness preservation. To preserve brightness, a trivial solution is to keep the original image without modification. Obviously, this violates the basic objective of image enhancement.

TABLE III

COMPARISON WITH OTHER RELATIVE WORKS. THE METRICS ARE DISCRETE ENTROPY (DE), ABSOLUTE MEAN BRIGHTNESS ERROR (AMBE), MEASUREMENT OF ENHANCEMENT (EME), AND TENENGRAAD CRITERION (TEN)

Evaluation Metrics	DE	AMBE	EME	TEN
HE [1]	5.910145	0.17537	6.986534	0.087381
2D hist [16]	6.09907	0.347427	9.469749	0.083417
SEGL[17]	7.200908	0.147956	6.636575	0.093428
HBLP [2]	6.879979	0.128545	6.969456	0.097866
GC [1]	7.52045	0.225797	11.06617	0.086737
AGC [4]	7.064793	0.174661	8.673812	0.097297
BF [20]	7.398008	0.000878	9.494262	0.138034
LL-SURE [25]	7.373331	0.00175	15.63878	0.38723
LCM [24]	7.375754	0.00135	7.803425	0.129104
TA [10]	7.448939	0.256015	11.06683	0.179773
Proposed method	7.633109	0.186175	20.55086	0.593348

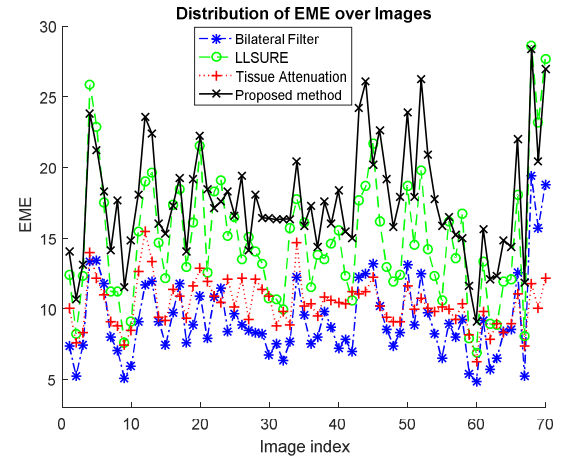


Fig. 12. The distribution of EME (measurement of enhancement) over 70 enhanced images produced by BF [20], LLSURE [25], TA [10], and our method. The X-axis is the image index; the y-axis is the EME metric value. Better viewed in color.

Therefore, our system treats brightness preservation as a soft constraint rather than the major goal. In Table III, the AMBE values of the three methods, BF [20], LLSURE [25], and LCM [24] are small. We could expect that the three methods would preserve brightness better than the rests. Accordingly, as given in Fig. 13(h) to Fig. 13(j), the enhanced results of the three methods has brightness similar to the original image. However, the details of these enhanced results are not distinct for X-ray inspection, especially in the bright regions. In contrast, our method enhances both the bright and dark regions with a fair AMBE value of 0.186.

As well as quantitative evaluation, we have provided the enhanced images output by the 11 methods (in Fig. 13) for visual comparison. First, we compared the difference between global adjustment methods and local adjustment methods. Without considering the local properties, the visualization of some local details produced by the global methods, such as

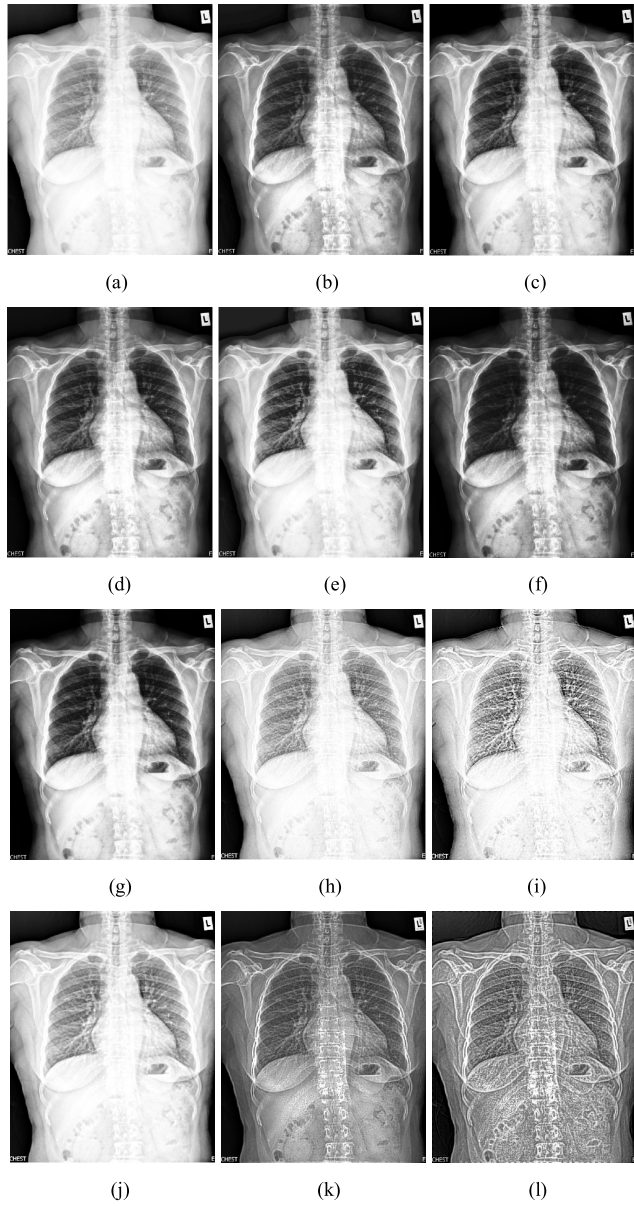


Fig. 13. The comparison of the 11 enhancement methods. (a) Original image. (b) HE [1] (Global). (c) GC [1] (Global). (d) SEGL [17]. (e) HBLP [2]. (f) 2D\_hist [16]. (g) AGC [4]. (h) BF [20]. (i) LL-SURE [25]. (j) LCM [24]. (k) TA [10]. (l) Proposed method.

Fig. 13 (b), Fig. 13(c), and Fig. 13(d), is not much improved. Although the global contrast is boosted, the dark regions still lack contrast and the details are difficult to figure out. In this example, the original chest X-ray image is over-bright. In order to stretch the dynamic range, the global methods tend to map a bright pixel to a darker one. In return, the details in bright regions become recognizable by sacrificing the dark regions. Thus it is challenging to preserve the details in both bright and dark regions by using a global adjustment method.

We then compared another 3 methods: HBLP [2], 2D\_Hist [16], and AGC [4]. They claim to enhance image global contrast and preserve local properties. HBLP [1] and 2D\_Hist [16] are the extensions of Histogram Equalization [1]; AGC [4] is a local adaptive version of gamma correction. Although these methods consider the local properties, the

quality of the result is not satisfactory for inspection. By evaluating Fig. 13(e) to Fig. 13(g), we cannot easily see the detail in the over-dark and over-bright regions. This may be because these methods are designed to keep the physical contrast order globally. In other words, the brightness in a dark region should still be smaller than a bright region after image enhancement. This assumption may be necessary for natural-looking enhancement. However, for X-ray inspection, the clearness of the details is more important than visual pleasure. To see the image details, methods that locally adjust images would be a better selection. Two such examples are the TA method and our proposed system. As we can see in Fig. 13(k) and Fig. 13(l), they are able to show details.

Some enhanced results produced by the transform-based methods of BF [20], LLSURE [25], and LCM [24] were also compared. These methods attempt to emphasize the high-frequency components in order to reveal image details; meanwhile, they preserve the low-frequency components so that the image brightness is preserved. The corresponding results of these methods are shown in Fig. 12(h) to Fig. 12(j). Overall, these methods increase visibility in the dark regions. However, the embedded details in the bright regions are still foggy. Unlike these methods, our method is specifically designed for X-ray inspection. How to present the details well is our primary goal. According to the results in Fig. 7, Fig. 11(c) and Fig. 13(l), we have demonstrated that our system can reveal the details of an X-ray image, not only in dark regions but also in bright regions.

### C. Application for Disease Inspection

Moreover, we hope to show our system is able to help doctors with disease inspection. Thus, we applied the proposed method to enhance the X-ray images in the JSRT dataset. In the dataset, some X-ray images have tiny nodules embedded in the chest area. Compared with the other X-ray dataset, the JSRT X-ray images are of lower resolution and lower contrast. In addition, due to the lower image quality, it is hard to recognize the locations of nodules without image enhancement.

Some JSRT X-ray images with and without enhancement are shown in Fig. 14. The known nodule locations are indicated by arrows. In the example, we cannot easily identify the nodules from the original X-ray image. After applying the proposed method to adjust the image contrast, Fig. 14(b) shows that the nodule regions become clearer. Even more, both the nodules and the bone structure are enhanced well. Moreover, the JSRT X-ray images are over-bright. Fig. 14(a) shows that we cannot clearly see the image contents in the bright and dark regions. After applying the proposed method, our system increases the image details by attenuating tissue components. The ensemble framework also makes our image enhancement locally adaptive to different image regions. Thus, our result in Fig. 14(b) shows that we can discover many small but significant details.

Besides, for comparison, we also include the results produced by the other 6 methods in Fig. 14. Similar to the discussion in Fig. 13, the proposed method can reveal more

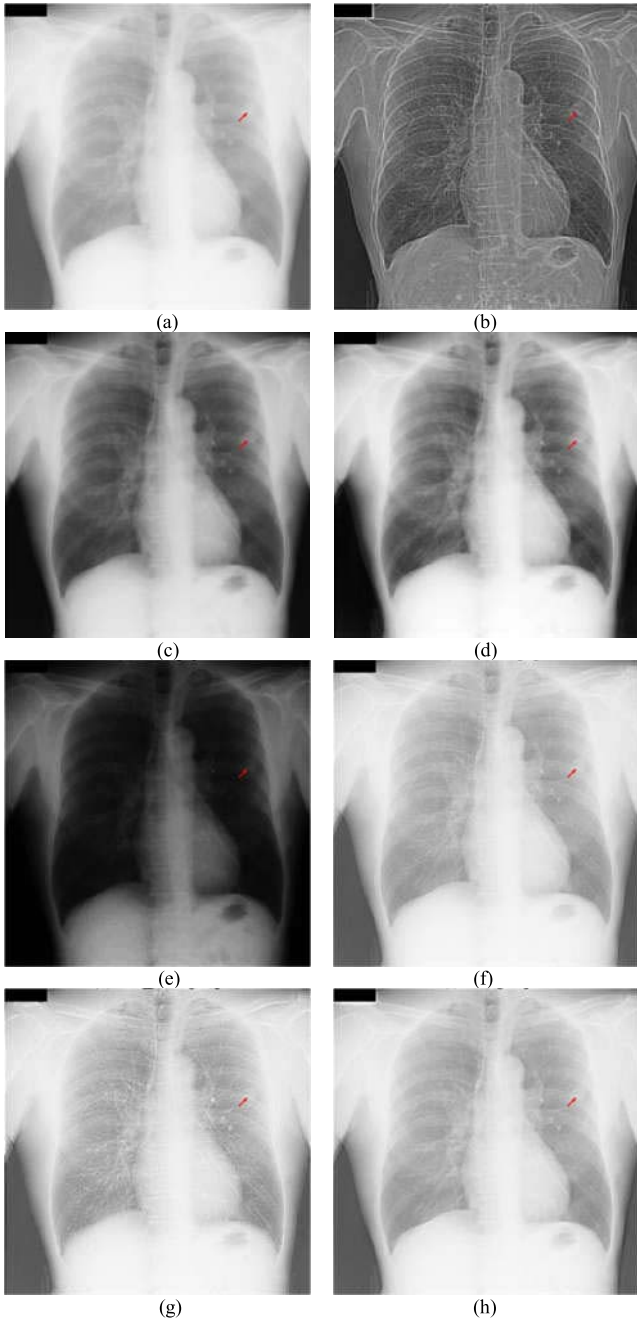


Fig. 14. The comparison of enhancement methods for nodule inspection. (a) Original Image. (b) Proposed method. (c) GC [1]. (d) HBLP [2]. (e) 2D\_hist. [16] (f) BF [20]. (g) LL-SURE. [25] (h) LCM [24].

structural details in both the dark regions and bright regions if compared with the other methods. Furthermore, to manually inspect the nodules from an X-ray image, a simplified principle is to find the blobs with circle shapes in the chest region. Since the proposed method is able to locally and adaptively enhance the boundaries of objects, the nodule boundaries also become sharper in our enhanced results. While using the proposed method to help with X-ray inspection, the radiologists can check the original X-ray image and our enhanced result simultaneously. On the one side, if the radiologist identifies a possible nodule in the original image, our enhanced image can help to verify the hypothesis and can provide a clearer view

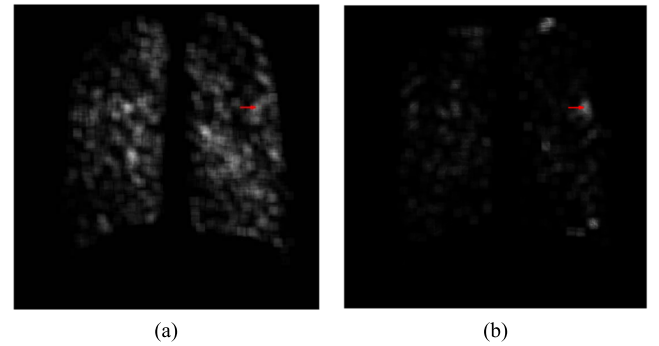


Fig. 15. The nodule-likeness maps generated from (a) the original image and (b) our enhanced image. The test image is same with Fig. 14. The small arrows show the locations of nodules.

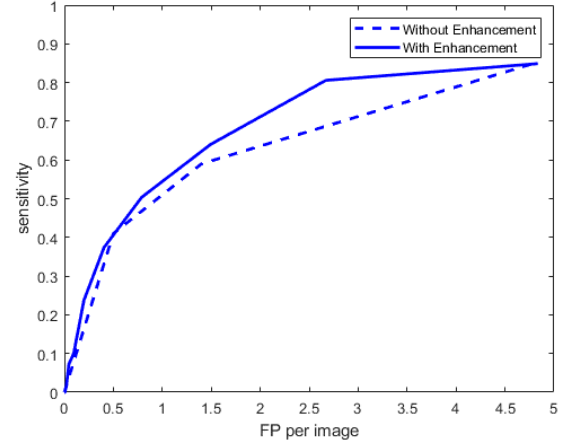


Fig. 16. The FROC curves of lung nodule detection with and without image enhancement. FP means false positives.

for the measurement of the nodule size. On the other side, the enhanced image is able to show the details which are not clear in the original image. This helps to reduce the number of missing detection. Therefore, the proposed method has two advantages in terms of nodule detection. First, our method can reveal more image details and reduce missing detection. Second, the sharper object boundaries help to locate nodules and make the measurement of nodule sizes easier.

In addition, to objectively compare nodule detection with and without the proposed enhancement method, we implement the nodule detection algorithm [41]. The method is chosen because it also uses JSRT dataset for experiments. The method is composed of three steps. First, the method extracts pixel-wise features based on filter banks. Second, the extracted features are inputted into a well-trained pixel-wise classifier to generate a nodule-likeness map. Finally, given the likeness map, a multi-scale blob detection algorithm is used to identify nodules in the image. In Fig. 15, we show the nodule-likeness maps generated from the original X-ray image and the enhanced image for comparison. Also, we compare the nodule detection performance with and without image enhancement by using Free-Response Receiver Operating Characteristic (FROC) [42] curves. The 140 JSRT X-ray images are all used for evaluation. As shown in Fig. 16, we achieve higher sensitivity and lower false positives when the proposed method is applied. These experiments and comparisons show that our enhanced images are useful for disease diagnosis.

## VII. CONCLUSION

The energy recorded in an X-ray image is able to reveal the internal condition of a human body. Thus, X-ray imaging has become a standard tool for health inspection. However, the low contrast property of an X-ray image makes it hard to recognize tiny and abnormal details. In this paper, a new enhancement system based on component attenuation, contrast adjustment, and image fusion was proposed. By attenuating the tissues over the image, we can enhance the essential details in both the bright and dark regions adaptively. Established in this concept, a novel parametric adjustment model was formulated. The model enables users to easily enhance image contrast by adjusting the attenuation scale. To locally enhance the contrast, an ensemble strategy was also proposed to fuse many enhanced images and generate the final output by maximizing the visual contrast. We have used four measurement metrics and two datasets to evaluate our system. The results demonstrated the effectiveness of our method to enhance organs, bone structure, and some small but significant details, such as tiny nodules in low contrast X-ray images. Moreover, an online testing system was also built for subjective evaluation. It showed that our system can help doctors with disease inspection.

## APPENDIX A

See Table IV.

## APPENDIX B INSIGHT INTO TISSUE ATTENUATION

It is worth discussing the role of the attenuation factor  $\alpha$  and its influences in the enhanced result  $E(x)$ . For analysis, we introduced the concept of local patch contrast ratio ( $LCR$ ) which is also known as Weber local contrast [31]. For a local patch of a normalized image  $I_n(x)$  around a pixel  $x$ , the  $LCR$  is defined in equation (A.1).

$$LCR(I_n(x)) \triangleq \frac{I_n^{\max}(x) - I_n^{\min}(x)}{I_n^{\min}(x)}. \quad (\text{A.1})$$

Note  $I_n^{\max}(x) \triangleq \max_{y \in L_x} I_n(y)$  and  $I_n^{\min}(x) \triangleq \min_{y \in L_x} I_n(y)$ ;  $L_x$  is the local region around a pixel  $x$ . Following the same definition, we can calculate the  $LCR$  of the enhanced image  $E(x)$  by:

$$LCR(E(x)) = \frac{E_n^{\max}(x) - E_n^{\min}(x)}{E_n^{\min}(x)}, \quad (\text{A.2})$$

where  $E_n^{\max}(x)$  and  $E_n^{\min}(x)$  are the local maximum and minimum of a local region around a pixel  $x$ . By referring to equation (3) and equation (4), we can derive  $E_n^{\max}(x)$  as:

$$\begin{aligned} E_n^{\max}(x) &\triangleq \max_{y \in L_x} E(y) = \max_{y \in L_x} \frac{I_n(y) - \alpha \cdot I_n^{\min}(y)}{I_n^{\max}(y)^{\lambda(y)} - \alpha \cdot I_n^{\min}(y)} \\ &\approx \frac{\left[ \max_{y \in L_x} I_n(y) \right] - \alpha \cdot I_n^{\min}(x)}{I_n^{\max}(x)^{\lambda(x)} - \alpha \cdot I_n^{\min}(x)} \\ &= \frac{I_n^{\max}(x) - \alpha \cdot I_n^{\min}(x)}{I_n^{\max}(x)^{\lambda(x)} - \alpha \cdot I_n^{\min}(x)}. \end{aligned} \quad (\text{A.3})$$

TABLE IV  
TABLE OF VARIABLE NOTATIONS

Notation	Description
$I_n(x)$	Normalization image
$I(x)$	Input image
$I_n^{\max}(x)$	Local maximum of a normalized image around an image pixel $x$
$I_n^{\min}(x)$	Local minimum of a normalized image around an image pixel $x$
$D(x)$	Detail component at the $x^{\text{th}}$ pixel
$R(x)$	Removing component at $x^{\text{th}}$ pixel
$T(x)$	Tissue component at $x^{\text{th}}$ pixel
$E(x)$	Enhanced image at the $x^{\text{th}}$ pixel
$E_n^{\min}(x)$	Local minimum of an enhanced image around an image pixel $x$
$E_n^{\max}(x)$	Local maximum of an enhanced image around an image pixel $x$
$\lambda(x)$	A local parameter to keep the brightness of a local region around pixel $x$
$\alpha$	A global parameter to control the attenuation ratio
$W_i(x)$	The fusion weight for the $i^{\text{th}}$ image at pixel $x$
$C_i(x)$	Contrast level of the $i^{\text{th}}$ image at pixel $x$
$BP_i(x)$	Brightness preserving of the $i^{\text{th}}$ image at pixel $x$
$D_i(x)$	Local maximum difference between the enhanced image $E_i(x)$ and the normalization image $I_n(x)$
$F(x)$	The final fusion output
$LCR(\cdot)$	Local patch contrast ratio function
$PCR_x$	The pixel-based contrast range at pixel $x$
$R^{LC}(x)$	The optimal local contrast at pixel $x$

In the above derivation, we have assumed that the local maximum and minimum of different pixels in a small local region  $L_x$  is roughly fixed. That is, we assumed  $I_n^{\min}(y) \approx I_n^{\min}(x)$  and  $I_n^{\max}(y) \approx I_n^{\max}(x)$  if  $y \in L_x$ . Furthermore, as shown in equation (6), the setting of  $\lambda^*(x)$  depends only on  $I_n^{\min}(x)$  and  $I_n^{\max}(x)$ . Thus, we have  $\lambda(y) \approx \lambda(x)$  for any pixel  $y \in L_x$ . Similarly, based on these assumptions,  $E_n^{\min}(x)$  is estimated by:

$$E_n^{\min}(x) \triangleq \min_{y \in L_x} E(y) \approx \frac{I_n^{\min}(x) - \alpha \cdot I_n^{\min}(x)}{I_n^{\max}(x)^{\lambda(x)} - \alpha \cdot I_n^{\min}(x)}. \quad (\text{A.4})$$

With the newly derived  $E_n^{\max}(x)$  and  $E_n^{\min}(x)$ , the  $LCR$  of the enhanced image  $E(x)$  defined in equation (A.2) can be rewritten as:

$$\begin{aligned} LCR(E(x)) &\approx \frac{I_n^{\max}(x) - I_n^{\min}(x)}{I_n^{\min}(x) - \alpha \cdot I_n^{\min}(x)} \\ &= \frac{1}{1 - \alpha} \left( \frac{I_n^{\max}(x) - I_n^{\min}(x)}{I_n^{\min}(x)} \right) \end{aligned} \quad (\text{A.5})$$

Now, from equation (A.1) and (A.5), we define enhancement ratio as:

$$EnhancementRatio(\alpha) \triangleq \frac{LCR(E(x))}{LCR(I_n(x))} = \frac{1}{1 - \alpha}. \quad (\text{A.6})$$

We find the attenuation factor  $\alpha$  can be regarded as a global parameter to control the enhancement ratio between  $E(x)$  and  $I_n(x)$  in terms of  $LCR$ . Over all image pixels, the ratio is fixed

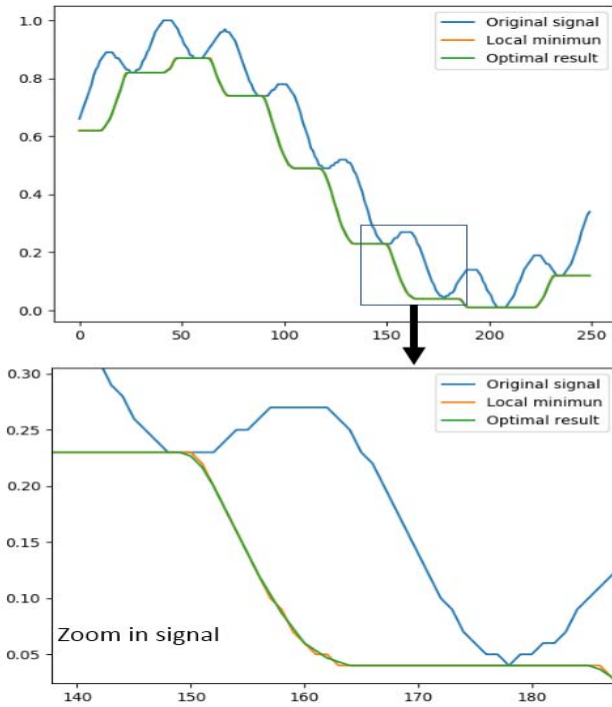


Fig. 17. A 1D test signal (blue) for the maximum removable component map estimation. The green distribution is the optimal solution with regularization. The orange distribution is the approximated solution using the local minimum within a window.

to  $\frac{1}{1-\alpha}$  once the  $\alpha$  value is selected. When  $\alpha$  increases from 0 to 1, the ratio rises accordingly.

#### APPENDIX C THE DERIVATION OF TISSUE ESTIMATION

In this appendix, we discuss how to estimate the maximum removable tissue component map  $T(x)$ . We assumed that  $T(x)$  can be determined by finding the optimal removable component map, which maximizes the summation of local contrast over the final enhanced image  $E(x)$ . In order to define the optimization problem, we introduced the pixel-based contrast range ( $PCR$ ) of  $E(x)$  at a pixel  $x$  as:

$$PCR_x \triangleq E(x) - \min_{y \in L_x} E(y), \quad (A.7)$$

where  $L_x$  represents the local region around the pixel  $x$ , and  $y$  is a pixel inside  $L_x$ . Also, some constraints are introduced in order to find a feasible estimation of the map  $T(x)$ . They include:

(a) Range Constraint:  $I_n(x) \geq R(x) \geq 0$  and  $R(x) \in N$  is a non-negative integer indicating the removable intensity at pixel  $x$ ;

(b) Smooth Neighborhood Constraint:  $\sum_{y \in L_x} (R(x) - R(y))^2$  should be small;

(c) Regularization Constraint: we prefer a larger  $R(x)^2$ . Note that the larger removable component we have, the higher contrast enhancement we can achieve.

Next, using equation (3), the map  $T(x)$  is then estimated by finding the removable component map  $R(x)$  that is subject

to the three constraints and maximizes the summation of  $PCR$  of the enhanced image  $E(x)$  over all image pixels. That is

$$T(x) \triangleq \operatorname{argmax}_R \sum_x \left\{ \begin{aligned} & \left[ E(x) - \min_{y \in L_x} E(y) \right]^2 + \gamma_1 [R(x)^2] \\ & - \gamma_2 \left[ \sum_{y \in L_x} (R(x) - R(y))^2 \right] \end{aligned} \right\} \\ \text{subject to } I_n(x) \geq R(x) \geq 0 \text{ and } R(x) \in N. \quad (A.8)$$

In (A.8),  $E(x)$  is a function of  $R(x)$ ;  $\gamma_1$  and  $\gamma_2$  are two tunable weights to control the importance of constraints. Since the optimal  $R(x)$  is highly related to its neighbors  $\{R(y)\}_{y \in L_x}$ , the solution to the optimization problem is non-trivial. To solve the problem, we apply the Graph Cut algorithm. A 1D test signal and its optimization result are shown in Fig. 17. We may find the optimal solution is close to the distribution of local minimum. This gives us the intuition to approximate the map  $T(x)$  by simply finding the local minimum within a local region around  $x$ . That is  $T(x) \cong \min_{y \in L_x} I_n(y)$ .

#### REFERENCES

- [1] P. Chaudhary, K. Shaw, and P. K. Mallick, "A survey on image enhancement techniques using aesthetic community," in *Proc. Int. Conf. Intell. Comput. Appl.*, 2017, pp. 585–596.
- [2] S.-D. Chen and A. R. Ramli, "Minimum mean brightness error bi-histogram equalization in contrast enhancement," *IEEE Trans. Consum. Electron.*, vol. 49, no. 4, pp. 1310–1319, Nov. 2003.
- [3] J.-Y. Kim, L.-S. Kim, and S.-H. Hwang, "An advanced contrast enhancement using partially overlapped sub-block histogram equalization," *IEEE Trans. Circuits Syst. Video Technol.*, vol. 11, no. 4, pp. 475–484, Apr. 2001.
- [4] S.-C. Huang, F.-C. Cheng, and Y.-S. Chiu, "Efficient contrast enhancement using adaptive gamma correction with weighting distribution," *IEEE Trans. Image Process.*, vol. 22, no. 3, pp. 1032–1041, Mar. 2013.
- [5] E. Land, "An alternative technique for the computation of the designator in the retinex theory of color vision," *Proc. Nat. Acad. Sci. USA*, vol. 83, no. 10, pp. 3078–3080, 1986.
- [6] D. J. Jobson, Z.-U. Rahman, and G. A. Woodell, "Properties and performance of a center/surround retinex," *IEEE Trans. Image Process.*, vol. 6, no. 3, pp. 451–462, Mar. 1997.
- [7] A. B. Petro, C. Sbert, and J.-M. Morel, "Multiscale retinex," in *Proc. Image Process. Line*, 2014, pp. 71–88.
- [8] S. Weizhen, L. Fei, and Z. Qinzheng, "The applications of improved retinex algorithm for X-ray medical image enhancement," in *Proc. Int. Conf. Comput. Sci. Service Syst.*, Aug. 2012, pp. 1655–1658.
- [9] K. He, J. Sun, and X. Tang, "Single image haze removal using dark channel prior," *IEEE Trans. Pattern Anal. Mach. Intell.*, vol. 33, no. 12, pp. 2341–2353, Dec. 2011.
- [10] C.-C. Huang, H.-N. Manh, and C.-Y. Tseng, "X-ray image contrast enhancement based on tissue attenuation," in *Proc. Int. Conf. Acoust., Speech Signal Process.*, May 2014, pp. 6602–6606.
- [11] S. Paris, P. Kornprobst, J. Tumblin, and F. Durand, "Bilateral filtering: Theory and applications," *Found. Trends Comput. Graph. Vis.*, vol. 4, no. 1, pp. 1–73, 2009.
- [12] A. Gandhamal, S. Talbar, S. Gajre, A. F. M. Hani, and D. Kumar, "Local gray level S-curve transformation a generalized contrast enhancement technique for medical images," *Comput. Biol. Med.*, vol. 83, pp. 120–133, Apr. 2017.
- [13] A. Jabeen, M. M. Riaz, N. Iltaf, and A. Ghafoor, "Image contrast enhancement using weighted transformation function," *IEEE Sensors J.*, vol. 16, no. 20, pp. 7534–7536, Oct. 2016.
- [14] T. Celik, "Two-dimensional histogram equalization and contrast enhancement," *Pattern Recognit.*, vol. 45, no. 10, pp. 3810–3824, Oct. 2012.
- [15] T. Celik and T. Tjahjadi, "Contextual and variational contrast enhancement," *IEEE Trans. Image Process.*, vol. 20, no. 12, pp. 3431–3441, Dec. 2011.
- [16] C. Lee, C. Lee, and C.-S. Kim, "Contrast enhancement based on layered difference representation of 2D histograms," *IEEE Trans. Image Process.*, vol. 22, no. 12, pp. 5372–5384, Dec. 2013.

- [17] T. Celik, "Spatial entropy-based global and local image contrast enhancement," *IEEE Trans. Image Process.*, vol. 23, no. 12, pp. 5298–5308, Dec. 2014.
- [18] T. Celik and L. Heng-Chao, "Residual spatial entropy-based image contrast enhancement and gradient-based relative contrast measurement," *J. Mod. Opt.*, vol. 63, no. 16, pp. 1600–1617, 2016.
- [19] D. H. Choi, I. H. Jang, M. H. Kim, and N. C. Kim, "Color image enhancement using single-scale retinex based on an improved image formation model," in *Proc. Eur. Conf. Signal Process.*, Aug. 2008, pp. 1–5.
- [20] F. Durand and J. Dorsey, "Fast bilateral filtering for the display of high-dynamic-range images," *ACM Trans. Graph.*, vol. 21, no. 3, pp. 257–266, 2002.
- [21] W. Wang, B. Li, J. Zheng, S. Xian, and J. Wang, "A fast multi-scale retinex algorithm for color image enhancement," in *Proc. Int. Conf. Wavelet Anal. Pattern Recognit.*, vol. 1, Aug. 2008, pp. 80–85.
- [22] J. Tang, X. Liu, and Q. Sun, "A direct image contrast enhancement algorithm in the wavelet domain for screening mammograms," *IEEE J. Sel. Topics Signal Process.*, vol. 3, no. 1, pp. 74–80, Feb. 2009.
- [23] X. Liu, J. Tang, S. Xiong, Z. Feng, and Z. Wang, "A multiscale contrast enhancement algorithm for breast cancer detection using Laplacian Pyramid," in *Proc. Int. Conf. Inf. Automat.*, Jun. 2009, pp. 1167–1171.
- [24] S. C. Nercessian, K. A. Panetta, and S. S. Agaian, "Non-linear direct multi-scale image enhancement based on the luminance and contrast masking characteristics of the human visual system," *IEEE Trans. Image Process.*, vol. 22, no. 9, pp. 3549–3561, Sep. 2013.
- [25] T. Qiu, A. Wang, N. Yu, and A. Song, "LLSURE: Local linear SURE-based edge-preserving image filtering," *IEEE Trans. Image Process.*, vol. 22, no. 1, pp. 80–90, Jan. 2013.
- [26] T.-H. Wang *et al.*, "Pseudo-multiple-exposure-based tone fusion with local region adjustment," *IEEE Trans. Multimedia*, vol. 17, no. 4, pp. 470–484, Apr. 2015.
- [27] C.-C. Huang, I. Leo, M.-X. Cai, and H. T. Vu, "HDR compression based on image matting Laplacian," in *Proc. IEEE Int. Conf. Consum. Electron.-Taiwan (ICCE-TW)*, May 2016, pp. 301–303.
- [28] T. Mertens, J. Kautz, and F. Van Reeth, "Exposure fusion: A simple and practical alternative to high dynamic range photography," *Comput. Graph. Forum*, vol. 28, no. 1, pp. 161–171, 2009.
- [29] W. Zhang and W.-K. Cham, "Gradient-directed multiexposure composition," *IEEE Trans. Image Process.*, vol. 21, no. 4, pp. 2318–2323, Apr. 2012.
- [30] P. J. Burt and E. H. Adelson, "The Laplacian pyramid as a compact image code," *IEEE Trans. Commun.*, vol. COM-31, no. 4, pp. 532–540, Apr. 1983.
- [31] B. Ortiz-Jaramillo, A. Kumcu, L. Platasa, and W. Philips, "Computing contrast ratio in images using local content information," in *Proc. IEEE Symp. Signal Process., Images Comput. Vis.*, Sep. 2015, pp. 1–6.
- [32] T. Mertens, J. Kautz, and F. Van Reeth, "Exposure fusion," in *Proc. 15th Pacific Conf. Comput. Graph. Appl.*, Oct./Nov. 2007, pp. 382–390.
- [33] C.-C. Huang and M.-H. Nguyen, *X-Ray Enhancement Demo*. Accessed: Feb. 6, 2018. [Online]. Available: <http://acm.ee.ccu.edu.tw/Demo.aspx?c=6>
- [34] C.-C. Huang and M.-H. Nguyen, *User Feedback Result*. Accessed: Feb. 6, 2018. [Online]. Available: <http://acm.ee.ccu.edu.tw/Demo.aspx?c=6>
- [35] C.-C. Huang and M.-H. Nguyen, *Survey*. Accessed: Feb. 6, 2018. [Online]. Available: <http://acm.ee.ccu.edu.tw/Demo.aspx?c=6>
- [36] C. E. Shannon, "A mathematical theory of communication," *Bell Syst. Tech. J.*, vol. 27, no. 3, pp. 623–656, Jul./Oct. 1948.
- [37] S. S. Agaian, B. Silver, and K. A. Panetta, "Transform coefficient histogram-based image enhancement algorithms using contrast entropy," *IEEE Trans. Image Process.*, vol. 16, no. 3, pp. 741–758, Mar. 2007.
- [38] Z. Chen, B. R. Abidi, D. L. Page, and M. A. Abidi, "Gray-level grouping (GLG): An automatic method for optimized image contrast Enhancement-part I: The basic method," *IEEE Trans. Image Process.*, vol. 15, no. 8, pp. 2290–2302, Aug. 2006.
- [39] J. Shiraishi *et al.*, "Development of a digital image database for chest radiographs with and without a lung nodule," *Amer. J. Roentgenol.*, vol. 174, no. 1, pp. 71–74, 2000.
- [40] Y. Zhang, G. Ji, and S. Wang, "A comprehensive survey on particle swarm optimization algorithm and its applications," *Math. Problems Eng.*, vol. 2015, Feb. 2015, Art. no. 931256.
- [41] X. Li, L. Shen, and S. Luo, "A solitary feature-based lung nodule detection approach for chest X-ray radiographs," *IEEE J. Biomed. Health Inform.*, vol. 22, no. 2, pp. 516–524, Mar. 2018.
- [42] D. P. Chakraborty, "Maximum likelihood analysis of free-response receiver operating characteristic (FROC) data," *Med. Phys.*, vol. 16, pp. 561–568, Jul. 1989.



**Ching-Chun Huang** (M'09) received the B.S., M.S., and Ph.D. degrees in electrical engineering from National Chiao Tung University, Hsinchu, Taiwan, in 2000, 2002, and 2010, respectively. He is currently an Associate Professor with the Department of Electrical Engineering, National Chung Cheng University, Taiwan. He is also leading the research lab, Applied Computing and Multimedia Lab. His research interests are in image/video processing, computer vision, machine learning, and wireless sensor networks.



**Manh-Hung Nguyen** received the B.S. and M.S. degrees in electrical engineering from the National University of Technology and Education, Ho Chi Minh, Vietnam, in 2009 and 2011, respectively, and the Ph.D. degree in electrical engineering from the National Kaohsiung University of Applied Sciences, Taiwan, in 2016. He is currently an Assistant Professor with the Department of Electrical Engineering, University of Technology and Education, and also a Post-Doctoral Researcher with the Department of Electrical Engineering, National Chung Cheng University, Taiwan. His research interests are in machine learning and data analysis.